Available online at www.sciencedirect.com
SCIENCE DIRECT®
Talanta 67 (2005) 438–448
Talanta
www.elsevier.com/locate/talanta

# Towards advanced chemical and biological nanosensors—An overview

Chanda Ranjit Yonzon [1], Douglas A. Stuart [1], Xiaoyu Zhang, Adam D. McFarland, Christy L. Haynes, Richard P. Van Duyne *

*Department of Chemistry, Northwestern University, 2145 Sheridan Road, Evanston, IL 60208-3113, USA*

Available online 2 August 2005

**Abstract**

This paper reviews recent developments in the design and application of two types of optical nanosensor, those based on: (1) localized surface plasmon resonance (LSPR) spectroscopy and (2) surface-enhanced Raman scattering (SERS). The performance of these sensors is discussed in the context of biological and chemical sensing. The first section addresses the LSPR sensors. Arrays of nanotriangles were evaluated and characterized using realistic protein/ligand interactions. Isolated, single nanoparticles were used for chemosensing and performed comparably to the nanoparticle array sensors. In particular, we highlight the effect of nanoparticle morphology on sensing response. The second section details the use of SERS sensors using metal film over nanosphere (MFON) surfaces. The high SERS enhancements and long-term stability of MFONs were exploited in order to develop SERS-based sensors for two important target molecules: a *Bacillus anthracis* biomarker and glucose in a serum protein mixture.


*Keywords:* Localized surface plasmon resonance; Surface-enhanced Raman scattering; Metal film over nanosphere; Nanosensor; Nanosphere lithography

## 1. Introduction

Nanotechnology and nanoscale materials are a new and exciting field of research. The inherently small size and unusual optical, magnetic, catalytic, and mechanical properties of nanoparticles not found in bulk materials permit the development of novel devices and applications previously unavailable. One of the earliest applications of nanotechnology that has been realized is the development of improved chemical and biological sensors. Remarkable progress has been made in the last two decades in the development of optical sensors and their utilization in environmental protection [1,2], biotechnology [3], medical diagnostics [4,5], drug screening [6], food safety [2,7], and security [8]. In this review, we will survey two types of optical sensors based on two different materials fabricated by nanosphere lithography (NSL). We have chosen examples that demonstrate the applicability of these types of sensors to both chemical and biological analysis.

Nanosphere lithographic techniques are easily used, yet surprisingly versatile and powerful tools for the design of nanoscale materials with size and shape tunable optical properties. The fabrication of arrays of triangular nanoparticles in the interstices between the elements of the nanosphere deposition mask and formation of metal film over nanosphere (MFON) structures by deposition of metal that completely covers the mask are the two most direct NSL procedures, and are shown in Fig. 1. Changing either the size of the nanospheres comprising the mask or the amount of metal deposited through or on the mask markedly changes the optical properties of the material, as summarized in Table 1. The frequency agile and readily tunable optical properties of both types of materials can be exploited in sensing schemes. One such optical sensor is based on the triangular nanoparticles and uses localized surface plasmon resonance (LSPR) based sensing. LSPR sensing capitalizes on the fact that noble metal nanoparticles exhibit a strong UV–vis extinction (absorption and Rayleigh scattering) band, and that the wavelength of maximum extinction is red-shifted by an increase in the dielectric constant and thickness of the material surrounding the nanoparticles [9–16]. The second type of sensor, based on the MFON structure, relies on the enhanced electromagnetic

* Corresponding author. Tel.: +1 847 491 3516; fax: +1 847 491 7713.
*E-mail address:* vanduyne@chem.northwestern.edu (R.P. Van Duyne).
[1] Authors contributed equally to this work.

0039-9140/$ – see front matter © 2005 Elsevier B.V. All rights reserved.
doi:10.1016/j.talanta.2005.06.039

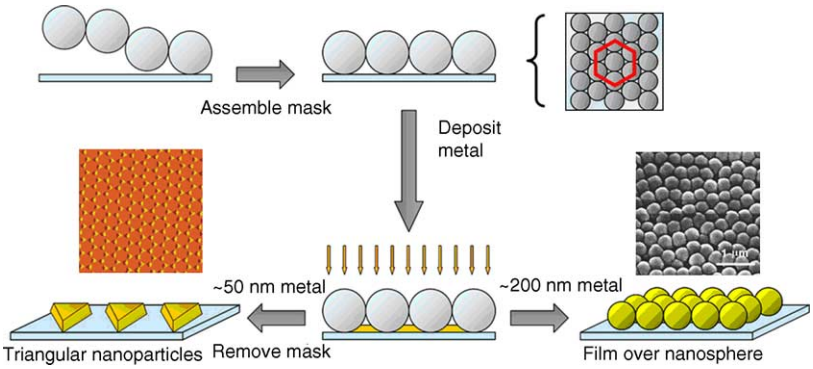


Fig. 1. Nanosphere lithographic fabrication of nanoparticle arrays and film over nanosphere surfaces.

fields generated by the characteristic surface roughness of the FON to produce strong and stable surface-enhanced Raman scattering (SERS) from target analytes.

## 2. Localized surface plasmon resonance sensing

LSPR sensors operate by transducing changes in local refractive index to wavelength shifts of the LSPR extinction band maximum (LSPR $\lambda_{max}$). The extinction band is a direct consequence of the excitation of the LSPR, which is a collective oscillation of the conduction electrons in the metal nanoparticle. LSPR excitation results in wavelength-selective absorption with extremely large molar extinction coefficients ($\sim 3 \times 10^{11}\ M^{-1}\ cm^{-1}$) [17], resonant Rayleigh scattering with efficiency equivalent to that of $10^6$ fluorophores [18,19], and enhanced local electromagnetic fields near the surface of the nanoparticle that are responsible for the intense signals observed in all surface-enhanced spectroscopies, e.g. SERS [20]. The LSPR $\lambda_{max}$, is dependent upon the size, shape, material, and dielectric environment of the nanoparticles [9–16]. The simplest theoretical model for the extinction, $E(\lambda)$ of spheroid shaped nanoparticles is given by Eq. (1):

$$E(\lambda) = \frac{24\pi^2 N a^3 \varepsilon_m^{3/2}}{\lambda \ln(10)} \left[ \frac{\varepsilon_i}{(\varepsilon_r + \chi\varepsilon_m)^2 + \varepsilon_i^2} \right] \quad (1)$$

where $N$ is Avagadro's number, $a$ the radius of the sphere, $\varepsilon_m$ the external dielectric constant, and $\varepsilon_i$ and $\varepsilon_r$ are the imaginary and real portion of dielectric constant of the metal [21]. The effects of particle shape are accounted for with the factor $\chi$, which has value of 2 for a perfect sphere, and increases directly with the nanoparticle's aspect ratio.

LSPR sensors and their more conventional counterpart, the propagating SPR sensor, have an inherent advantage over other optical biosensors that require a chromophoric group or other label to transduce the binding event. The response of LSPR and SPR sensors is proportional to the product of adsorbate, thin layers, and refractive index. Furthermore, if properly functionalized with appropriate receptor molecules (e.g. antibodies), they require very little ligand purification due to the specific ligand/receptor binding of these molecules. Also, these sensors provide real-time information [22] on the course of binding and are applicable over a broad range of binding affinities. The sensing capability of LSPR sensors can also be tuned by changing the shape, size, and material composition of the nanoparticles [9,23]. Additionally, LSPR sensing elements are inherently the size of a single nanoparticle, making the LSPR sensors potentially applicable for in vivo detection in biological cells.

Table 1
Comparative LSPR $\lambda_{max}$ values for varying sphere mask sizes ($D$) and metal deposition thicknesses ($d_m$)

| $D$ (nm) | $d_m$ (nm) | $\lambda_{max}$ (nm) |
|---|---|---|
| NSL-fabricated Ag nanotriangles | | |
| 390 | 40 | ~620 |
| 390 | 50 | ~580 |
| 390 | 50 | ~580 |
| 510 | 50 | ~710 |
| 590 | 50 | ~860 |
| 1100 | 50 | ~1360 |
| NSL-fabricated MFON | | |
| 390 | 200 | ~530[a] |
| 510 | 200 | ~680[a] |
| 600 | 200 | ~750[a] |

[a] Denotes values for $\lambda_{min}$ (nm).

### 2.1. Ensemble nanosensors for carbohydrate binding protein (Concanavalin A)

NSL-fabricated Ag nanotriangles with out-of-plane heights of 50 nm and in-plane widths of ~100 nm on a glass substrate were placed in a mixture of tri(ethylene glycol) disulfide and maleimide-terminated disulfide to present about 5% of the maleimide on the surface. The substrate was rinsed with ethanol and placed in a flow cell after exposure to mannose. The LSPR spectrum of the mannose-functionalized Ag nanosensor had a LSPR $\lambda_{max}$ of 662.4 nm (Fig. 2A). Then, 19.8 μM Concanavalin A (Con A) was injected into the flow cell and the Ag nanosensor was incubated at room temperature for 20 min to ensure complete binding. The sample was

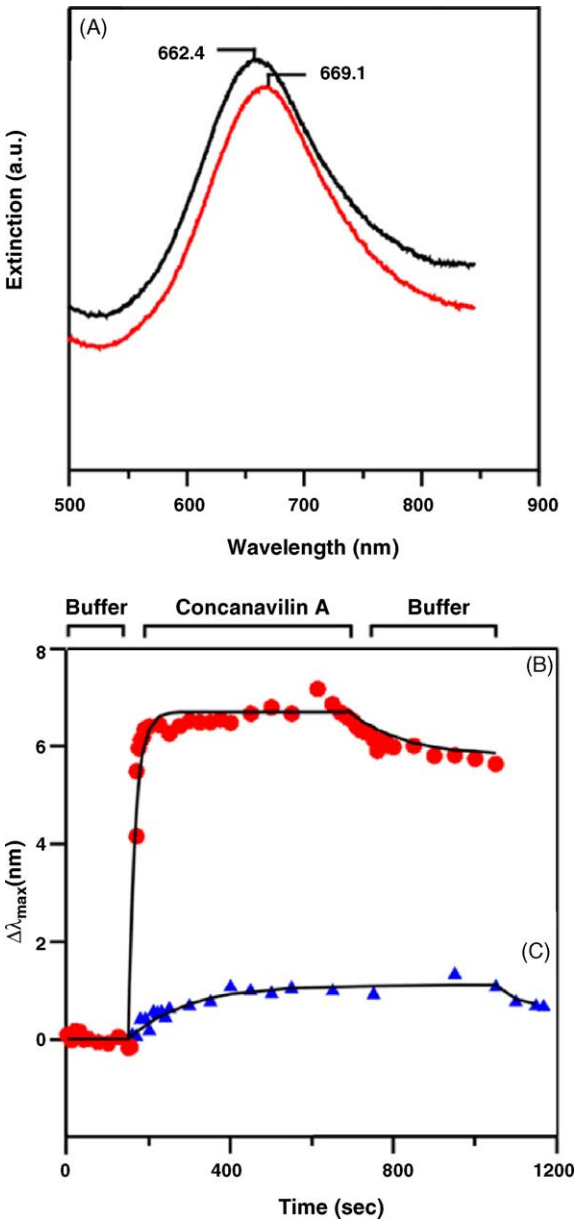


Fig. 2. (A) LSPR spectra of mannose-functionalized Ag nanosensor ($\lambda_{max}$ = 662.4 nm) and the specific binding of ConA to mannose ($\lambda_{max}$ = 669.1 nm) in PBS buffer. Real-time response of (B) mannose and (C) galactose-functionalized LSPR sensor as 19 μM of ConA was injected in the cell following buffer injection.

thoroughly rinsed in buffer solution, and the LSPR $\lambda_{max}$ of the Ag nanotriangles was measured to be 669.1 nm, a 6.7 nm red-shift of the LSPR $\lambda_{max}$. Furthermore, real-time binding studies were performed on a mannose-functionalized LSPR sensor (Fig. 2B). ConA (19 μM) in buffer was injected after the baseline LSPR $\Delta\lambda_{max}$ response of the mannose-functionalized Ag nanotriangles in a running buffer environment was recorded. The sensor was then flushed with buffer to remove any non-specifically bound ConA and weakly bound protein/sugar complexes. During this process, the LSPR $\lambda_{max}$ was measured in 5 s intervals for 20 min. Note that the spike of $\Delta\lambda_{max}$ at 500 s in Fig. 2B is caused by flow non-uniformity (noise) due to manual injection.

During the association phase, the LSPR sensor showed a rapid response when ConA was exposed to the surface, which indicates strong mannose/ConA interaction on the surface [24] followed by weak non-specific binding. However, during the dissociation phase, the signal decreased by 14%. The dissociation response seen is attributable to the removal of non-specifically bound ConA and partial dissociation of bound ConA.

A similar real-time experiment was performed to observe the binding of ConA to a galactose-functionalized Ag nanosensor (Fig. 2C). To illustrate that ConA has very little affinity toward galactose, a 5% galactose-functionalized surface was exposed to 19 μM ConA. After the wash with PBS buffer, the LSPR sensor showed a very small $\Delta\lambda_{max}$. This small response was previously observed when fluorescently labeled ConA was exposed to a galactose-functionalized surface [25].

### 2.2. LSPR response with respect to the height of Ag nanotriangles

The size of the Ag nanoparticles governs not only the initial LSPR $\lambda_{max}$ [9], but also the magnitude of the LSPR response. A study to understand the LSPR response with respect to nanoparticle height was performed using arrays of Ag nanoparticles with various out-of-plane heights, but fixed in-plane widths. Arrays with out-of-plane heights of 16, 25, and 50 nm were fabricated, and functionalized with mannose. The nanoparticle arrays were placed in a flow cell with PBS buffer solution, then 19 μM ConA was injected followed by rinsing with buffer to remove weakly bound ConA. Mannose-functionalized Ag nanosensors with 16 nm (Fig. 3A), 25 nm (Fig. 3B), and 50 nm (Fig. 3C) out-of-plane height gave LSPR $\lambda_{max}$ of 808.3, 707.2, and 662.4 nm, respectively. When the mannose-functionalized surface of these nanotraingles were exposed to ConA, $\lambda_{max}$ shifts of 22.2 nm (−0.041 eV), 11.4 nm (−0.027 eV), and 6.7 nm (−0.022 eV) was seen, and 19.1 nm (−0.035 eV), 9.6 nm (−0.023 eV), and 5.8 nm (−0.016 eV) net response when weakly bound ConA was removed by washing the sample with the PBS buffer. In all cases, the areal density of ConA molecules bound to the mannose-functionalized surface was identical, however, the overall response of the nanosensor increased with decreasing nanoparticle height. Furthermore, when the ConA bound nanosensors were rinsed with buffer, the change in the response increased as the nanoparticle height decreased.

To explore the mechanism behind the experimental results in Fig. 3, the discrete dipole approximation (DDA) method [26–28] was used. The theoretical calculations shows [22] qualitative agreement with experimental data; as Ag nanoparticle height increases, the aspect ratio of the nanoparticle decreases, and $\Delta(\Delta\lambda_{max})$ decreases. The trend seen in Fig. 3 can also be explained by consideration of the characteristic length of the electromagnetic field decay, $l_d$, at the

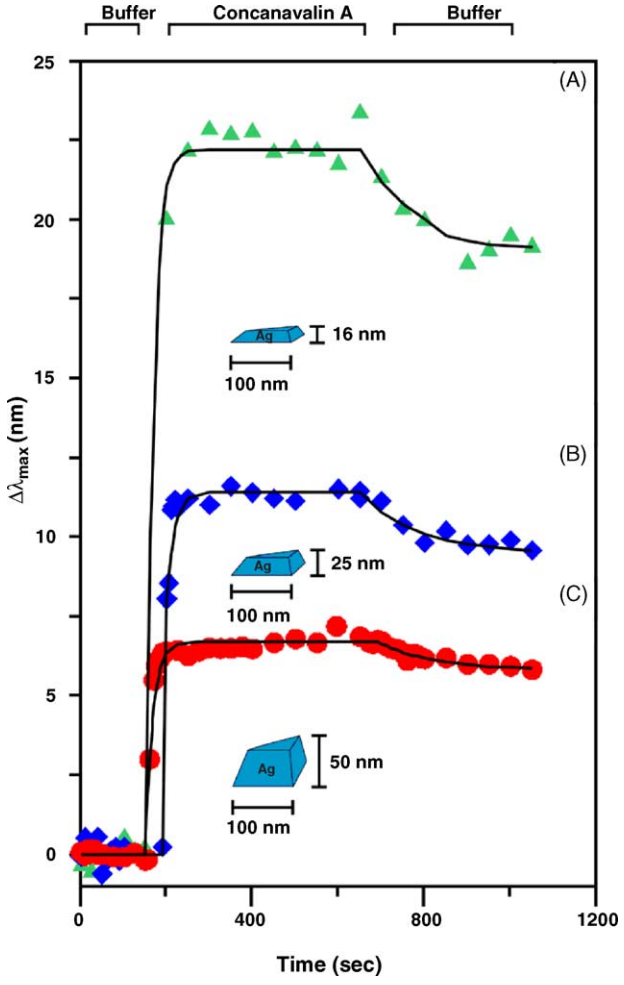


Fig. 3. Real-time response of mannose-functionalized Ag nanosensor as 19 μM of ConA was injected in the cell following buffer injection: (A) 16 nm out-of plane height, (B) 25 nm out-of plane height, and (C) 50 nm out-of plane height. The solid lines are guides to the eye.

nanoparticle surface. Although the electromagnetic fields around nanoparticles are known to be more complex, a reasonable approximation for $l_d$ is 5–6 nm for a Ag nanoparticle with an in-plane width of 100 nm and out-of-plane height of 50 nm [16,29]. In addition, as the aspect of the nanoparticle increase, $l_d$ increases. Because $l_d$ for nanoparticles is significantly smaller than the size of ConA, the $\Delta\lambda_{max}$ response observed upon ConA binding is caused only by the portion of the ConA molecule in close proximity to the nanoparticle surface. In contrast, $l_d$ for SPR is known to be ~200 nm [30]. This longer decay length not only provides sensitivity beyond the specifically bound molecules at the metal surface, but also results in a larger response when weakly bound ConA is washed away.

### 2.3. Sensing with single nanoparticles

The extension of the LSPR sensing technique to the single nanoparticle limit provides several advantages over existing array- or cluster-based techniques. First, absolute detection limits can be dramatically reduced. The surface area of chemically prepared Ag nanoparticles is typically less than 20,000 $nm^2$; therefore, a complete monolayer of adsorbate constitutes fewer than ~100 zeptomoles. The formation of alkanethiol monolayers on Ag nanoparticles can result in LSPR shifts of greater that 40 nm, a change that is over 100 times greater than the resolution of convention UV–vis spectrometers. This suggests that the limit of detection for single nanoparticle-based LSPR sensing will be well below 1000 molecules for small molecule adsorbates. The single molecule detection limit may be achievable for larger molecules, such as antibodies and proteins, that produce large changes in the local dielectric environment upon adsorption. Second, the extreme sensitivity of single nanoparticle sensors dictates that only very small sample volumes (viz., attoliters) are necessary to induce a measurable response. This characteristic could eliminate the need for analyte amplification techniques (e.g., polymerase chain reaction) required by other analytical methods. Third, single nanoparticle sensing platforms, like nanoparticle arrays, are readily applicable to multiplexed detection schemes by controlling the size, shape, and chemical modification of individual nanoparticles. Several nanoparticles with unique spectral responses can then be incorporated into one device, allowing for the rapid, simultaneous detection of many different chemical or biological species.

The key to exploiting single nanoparticles as sensing platforms is developing a technique to monitor the LSPR of individual nanoparticles with a reasonable signal-to-noise ratio. UV–vis absorption spectroscopy does not provide a practical means of accomplishing this task. Even under the most favorable experimental conditions, the absorbance of a single nanoparticle is very close to the shot noise-governed limit of detection. Instead, resonant Rayleigh scattering spectroscopy is the most straightforward means of characterizing the optical properties of individual metallic nanoparticles. Similar to fluorescence spectroscopy, the advantage of scattering spectroscopy lies in the fact that the scattering signal is detected against a very low background. The instrumental approach for performing these experiments generally involves using high magnification microscopy coupled with oblique or evanescent illumination of the nanoparticles. This has been most commonly achieved with dark-field transmission spectroscopy [31–33], but can also be realized with near-field scanning optical microscopy [34], or differential interference contrast microscopy [35].

Colloidal Ag nanoparticles were prepared by reducing silver nitrate with sodium citrate in aqueous solution according to the procedure referenced above [36]. Immobilized particles on cover slips were inserted into a flow cell and were exposed to various dielectric environments or molecular adsorbates [37]. Prior to all experiments, the nanoparticles in the flow cell were repeatedly rinsed with methanol and dried under nitrogen. All optical measurements were performed using an inverted dark-field microscope equipped with an imaging spectrograph. An image of a field of nanoparticles acquired

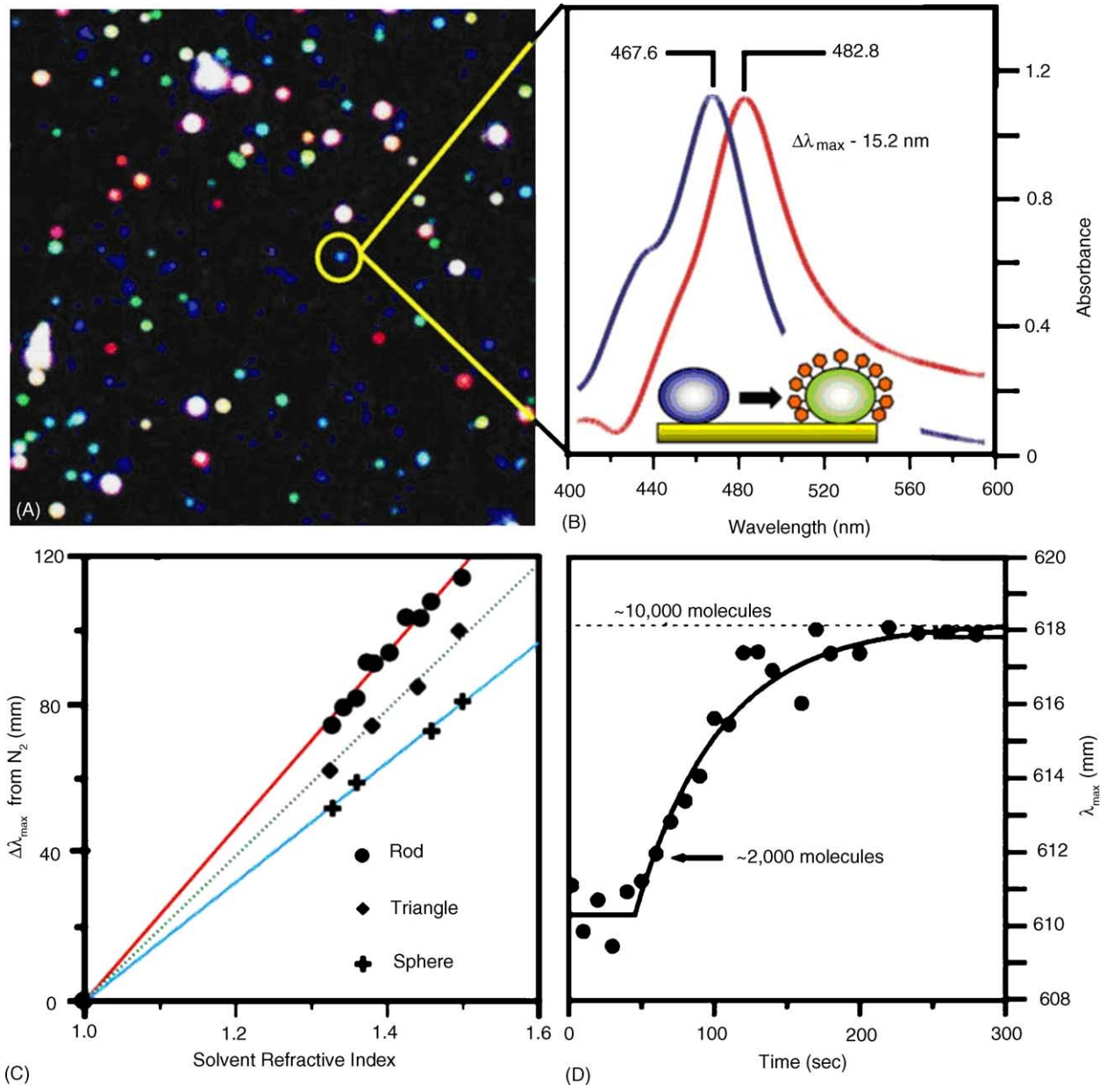


Fig. 4. Single nanoparticle spectroscopy and kinetics. (A) Dark-field image of silver nanoparticles; (B) representative spectra showing shift in LSPR on exposure of analyte; (C) shape effect with increasing solvent refractive index; (D) real-time binding kinetics.

with the apparatus is shown in Fig. 4A. Spatial filtering allows the spectral response of a target nanoparticle to be monitored (Fig. 4B).

The local refractive index sensitivity of the LSPR of a single Ag nanoparticle was measured by recording the resonant Rayleigh scattering spectrum of the nanoparticle as it was exposed to various solvent environments inside the flow cell. As illustrated in Fig. 4C, the LSPR $\lambda_{max}$ systematically shifts to longer wavelength as the solvent refractive index unit (RIU) is increased. Linear regression analysis for this nanoparticle yielded a refractive index sensitivity of 203.1 nm $RIU^{-1}$. The refractive index sensitivity of several individual Ag nanoparticles was measured and typical values were determined to be 170–235 nm $RIU^{-1}$. Fig. 4C also shows that the shape of the nanoparticles has a dramatic effect on the sensitivity of the LSPR response to changes in refractive index. Generally, the higher is the particle's aspect ratio, $\chi$, the larger the change in LSPR $\lambda_{max}$. The spherical particle has a sensitivity of 161 nm $RIU^{-1}$, the triangular nanoparticle has a sensitivity of 197 nm $RIU^{-1}$, and finally, the rod-like nanoparticle has a sensitivity of 235 nm $RIU^{-1}$ [37]. The triangular nanoparticle was fabricated using NSL, removed from its original substrate, and immobilized on a glass coverslip to ensure adequate interparticle separation. The geometries of the chemically synthesized nanoparticles were assigned on the basis of the LSPR

$\lambda_{max}$, line shape, and polarization dependence of the scattering spectra as well as similar assignments made by Mock et al. using TEM-correlated optical measurements [38]. These results are similar to the values obtained from experiments utilizing arrays of NSL-fabricated triangular nanoparticles [22,39,40]. Additionally, kinetic responses were monitored and were found to be competitive with other real-time sensors (Fig. 4D). Using the flow cell described above, immobilized single nanoparticles were exposed to a solution containing 1.0 mM 1-octanethiol. An analysis of the data reveals that the response exhibits first-order kinetics with a rate constant of $0.0167\,s^{-1}$, with saturation of the binding surface at about 10,000 molecules, and a limit of detection of ~2000 molecules.

## 3. Surface-enhanced Raman scattering (SERS) nanosensors

Vibrational spectroscopic methods are valuable analytical tools because they yield not only quantitative information but also unique vibrational signatures for small molecule analytes. Raman spectroscopy, in all its forms, is a vibrational spectroscopic method that has the inherent ability to distinguish between molecules with great similarity, such as the structural isomers glucose and fructose [41]. Unfortunately, high laser powers and long acquisition times are usually required to achieve high quality Raman spectra due to the inherently small normal Raman scattering (NRS) cross-section of many molecules of interest [42]. Higher intensity Raman signals and lower detection limits can be achieved using SERS. SERS produces very large enhancements in the effective Raman cross-section of species spatially confined within zone of the electromagnetic fields (viz., 0–4 nm) [43] generated upon excitation of the LSPR (described above) of nanostructured noble metal surfaces. This large electromagnetic field induces a dipole in nearby molecules, thus enhancing Raman scattering from absorbed molecules. The Raman signals of ensemble-averaged molecules show enhancement of up to 8 orders of magnitude [44], while the signals from single molecules can show an increase by 14–15 orders of magnitude in special cases [45,46]. In comparison with infrared absorption and NRS spectroscopies, SERS enjoys the advantages of application in aqueous media and the sensitivity sufficient for trace level detection [47]. This enables SERS spectroscopy to be one of the most effective trace analytical methods. Although SERS intensity varies from sample to sample due to the substrate morphology, by choosing an appropriate internal standard or developing a large calibration data set, SERS can be used for quantitative detection. The distinct advantages of SERS, such as low detection limit, real-time response, both qualitative and quantitative analysis capabilities, a high degree of specificity, and simultaneous multi-component detection, make it applicable in identification and characterization of pharmaceuticals, [48] bacteria [49], and other molecular species [50].

For sensors, it is important that the optical properties of the substrate be designed to fully maximize SERS intensities, which accordingly lower the analytical limit of detection (LOD). Early SERS substrates contained a random distribution of roughness feature sizes produced by oxidation–reduction cycling on a metal electrode [51] or evaporation of a thin metal film onto a flat substrate [52]. In recent years, researchers have explored the optimal size, shape, spacing, and pattern of noble metal nanoparticles on surfaces to optimize SERS enhancements. One of the most robust SERS substrates in use today is the metal film over nanospheres substrates prepared by NSL (Fig. 1) [53–55]. The diameter of the colloidal nanosphere cores and the thickness of the metal film shell determine the size distribution of the roughness features and, hence, the optical response. Even though the nanoscale roughness features are not homogeneous in size; but are instead driven by the larger scale templating, they are homogeneous enough to generate a relatively narrow LSPR (FWHM ~ 200 nm). Recent experiments have conclusively demonstrated that MFON substrates are stable for weeks [56] (unlike many other nanostructured surfaces) and remain SERS-active even when exposed to large temperature [57] and potential excursions [54]. The utility of the MFON substrate is demonstrated herein as a robust SERS substrate used in biowarfare agent [56] and glucose detection [4,58].

### 3.1. Bacillus spore detection based on SERS

SERS has been successfully exploited in the rapid detection of *Bacillus subtilis* spores, harmless simulants for *B. anthracis* (Fig. 5A). A bacillus spore structurally consists of several protective layers and a core cell. CaDPA exists in these protective layers (Fig. 5B) and can be used as the spore biomarker because other potentially interfering species lack this particular molecule in such high proportions [59,60]. CaDPA was extracted from spores by sonicating a spore suspension in 0.02 M $HNO_3$ solution for 10 min. A $3.1 \times 10^{-13}$ M spore suspension ($3.7 \times 10^4$ spores in 0.2 μL, 0.02 M $HNO_3$) was deposited onto an AgFON substrate for the SERS measurement. A high signal-to-noise ratio (S/N) SERS spectrum was obtained in a 1-min data acquisition period (Fig. 5C); this spectrum is dominated by bands associated with CaDPA (Fig. 5D) as seen in previous Raman studies on bacillus spores [61]. The bands due to $HNO_3$ in the suspension were identified as well (Fig. 5E). The peak at $1050\,cm^{-1}$ in Fig. 5D is from the symmetrical stretching vibration of $NO_3^-$ [62,63]. Because of its prominence, this peak is used as an internal standard to reduce the sample-to-sample deviations.

The SERS signal from extracted CaDPA was measured over the spore concentration range $10^{-14}$–$10^{-12}$ M to determine the saturation binding capacity of the AgFON surface and to calculate the adsorption constant ($K_{spore} = 1.7 \times 10^{13}\,M^{-1}$). In Fig. 6A, each data point represents the average intensity at $1020\,cm^{-1}$ (a ring breathing

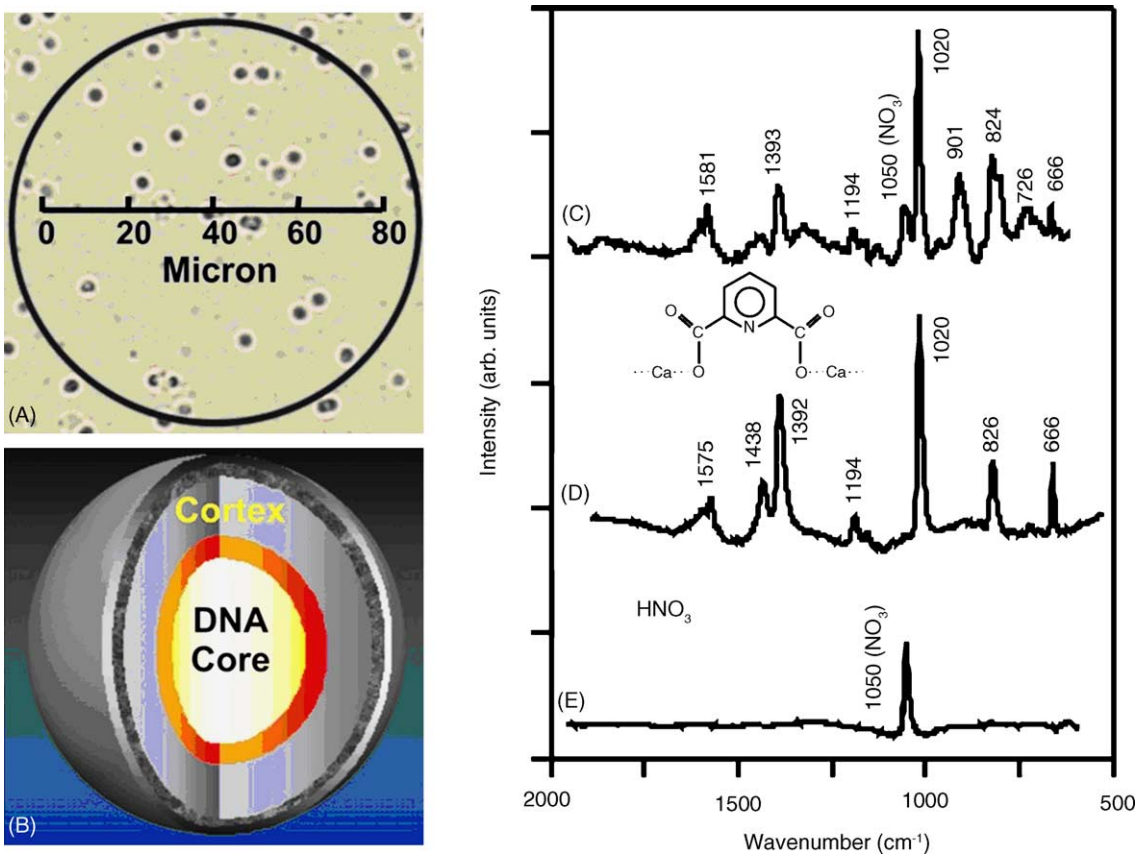


Fig. 5. Anthrax sensing. (A) Localization of dipicolinic acid within *Bacillus* spores; (B) structure (inset); (C) SERS spectrum of $3.1 \times 10^{-13}$ M spore suspension on a AgFON substrate; (D) SERS spectrum of $5.0 \times 10^{-4}$ M CaDPA; (E) SERS spectrum of 0.2 μL 0.02 M $HNO_3$. $\lambda_{ex} = 750$ nm, $P_{ex} = 50$ mW, and acquisition time = 1 min.

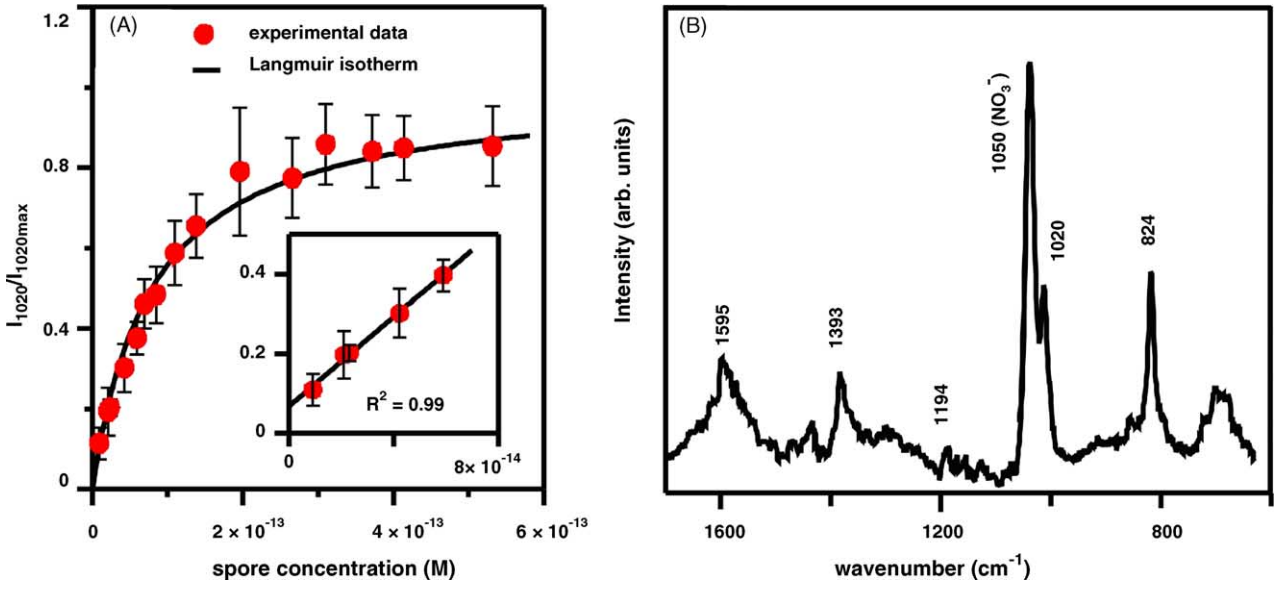


Fig. 6. (A) Adsorption isotherm for *Bacillus subtilis* spore suspension onto a AgFON substrate. $I_{1020}$ was taken from SERS spectra that correspond to varying spore concentrations in 0.2 μL, 0.02 M $HNO_3$ on AgFON substrates. $\lambda_{ex} = 750$ nm, $P_{ex} = 50$ mW, acquisition time = 1 min, $D = 600$ nm, and $d_{Ag} = 200$ nm. A Langmuir curve was generated with the adsorption constant for CaDPA from spores, $K_{spore} = 1.3 \times 10^{13}$ $M^{-1}$. The inset shows the linear range that is used to determine the LOD. Each data point represents the average value from three SERS spectra. Error bars show the standard deviations. (B) SERS spectrum of $2.1 \times 10^{-14}$ M spore suspension ($2.6 \times 10^3$ spores in 0.2 μL, 0.02 M $HNO_3$) on AgFON. $\lambda_{ex} = 750$ nm, $P_{ex} = 50$ mW, and acquisition time = 1 min.

mode) from three samples with the standard deviation shown by the error bars. At low spore concentrations, the peak intensity increases linearly with concentration (Fig. 6A inset). At higher spore concentrations, the response saturates as the adsorption sites on the AgFON substrate become fully occupied.

A SERS-based detection system must have the ability to detect less than the life-threatening dose of a pathogen in real or near-real-time in order to monitor bio-agents or other harmful species. Herein, the LOD is defined as the concentration of spores for which the strongest SERS signal of CaDPA at 1020 $cm^{-1}$ is equal to three times the background SERS signal within a 1-min acquisition period. The background signal refers to the SERS intensity from a sample with a spore concentration equal to zero, which is theoretically predicted to be the intercept of the low concentration end of the spore adsorption isotherm (Fig. 6A, inset). Although lower detection limits can be achieved by using longer acquisition times or higher laser power, the chosen parameters are reasonable for high throughput, real-time, and on-site analysis of potentially harmful species. The LOD for *B. subtilis* spores was found to be $2.1 \times 10^{-14}$ M ($2.6 \times 10^3$ spores in 0.2 μL, 0.02 M $HNO_3$), as calculated by extrapolation of the linear concentration range of the adsorption isotherms. Furthermore, a similar spore concentration $2.1 \times 10^{-14}$ M was used to test the LOD prediction. A 1-min acquisition yields a SERS spectrum that clearly demonstrates the spore Raman features (Fig. 6B) in comparison with Fig. 5A. These data demonstrate that the SERS LOD is well below the anthrax infectious dose of $10^4$ spores [64].

### 3.2. Glucose detection with SERS

While the CaDPA biomarker in *B. subtilis* spores has an affinity towards the rough noble metal surfaces required for SERS detection, many important molecules (e.g. glucose) lack an affinity towards such surfaces [58]. The work presented below demonstrates quantitative glucose detection by tailoring a SERS-active substrate with a self-assembled monolayer (SAM). All efforts to detect glucose on bare MFON surfaces using SERS were unsuccessful. Since the normal Raman cross-section of glucose should provide sufficient signal to be detected under surface-enhanced conditions [42], the inability to detect glucose using SERS must be attributed to the weak or non-existent binding of glucose to bare silver or gold surfaces. To bring glucose within the range of the enhanced electromagnetic fields around the FON surface, a SAM can be formed on the surface that can partition the analyte of interest (Fig. 7) [58] in a manner analogous to chromatographic stationary phases [65–69]. Functionalizing the MFON substrate with a partition layer has three advantages: (1) the SAM helps stabilize the surface against oxidation; (2) the SAM is exceedingly stable; (3) chemical selectivity and functionality is intrinsic and tailorable through synthetic control of the partition layer.

In initial experiments, several SAMs were tested to determine their effectiveness as a partition layer. Of these, only the straight chain alkanethiols were found to be effective partition layers, especially 1-decanethiol, 1-DT (which forms a monolayer on Ag ~ 1.9 nm thick) [70]. Although 1-DT was an effective partition layer for quantitative detection in the physiologically relevant concentration range (0–25 mM) [58], an ethylene glycol SAM has proven to be more effective [4]. The (1-mercaptoundeca-11-yl) tri(ethylene glycol), EG3, was chosen as a partition layer because of its ability to reject non-specific binding by background proteins [71–74] and its biocompatibility [75,76], progressing toward the long-term goal of fabricating an implantable glucose sensor. Each EG3-modified MFON sample was incubated in a flow cell with a glucose/saline solution (0–25 mM; 0–450 mg/dL) at a physiological pH (7.4). SERS spectra were then measured through an optical window in the cell. The spectra were normalized using EG3's S–C (~700 $cm^{-1}$) peak intensities, followed by chemometric (partial least squares) analysis. The resulting cross-validated glucose concentration predictions are presented on a Clarke error grid (Fig. 8).

The Clarke error grid is an established metric for evaluating glucose sensor efficacy in the clinical concentration range [77]. It is divided into five zones: zone A predictions lead to clinically correct treatment decisions; zone B predictions lead to benign errors or no treatment; zone C predictions lead to overcorrecting acceptable blood glucose concentrations; zone D predictions lead to dangerous failure to detect and

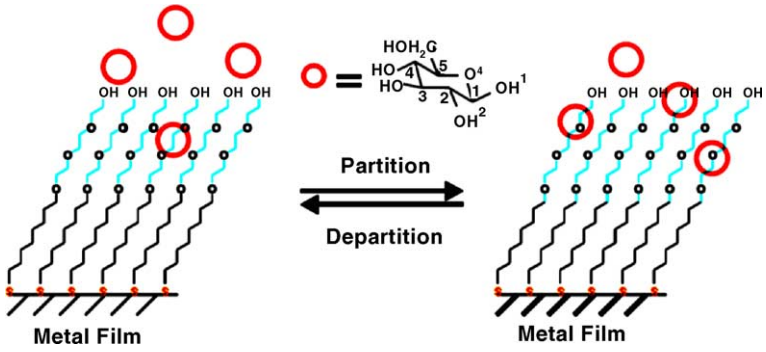


Fig. 7. Cartoon of monolayer functionalized FONs partitioning glucose molecules.

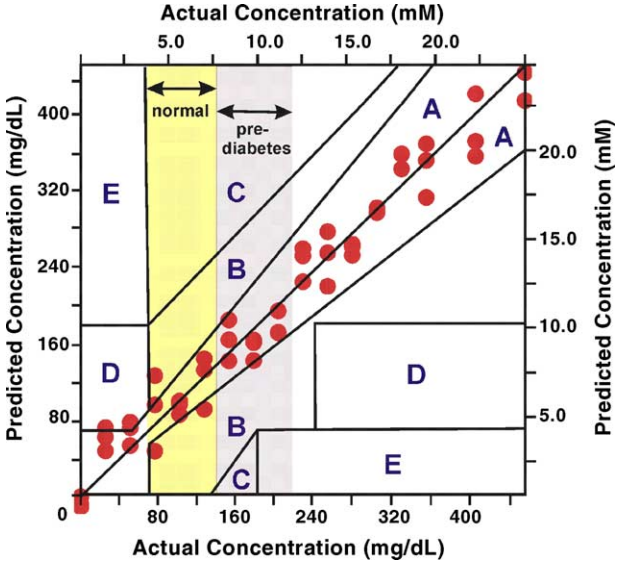


Fig. 8. Clarke error grid of LOO-PLS predicted glucose concentration versus actual glucose concentration (five loading vectors). AgFON samples were made ($D$ = 390 nm, $d_m$ = 200 nm), incubated for ~16 h in 1 mM EG3 solution, and dosed in glucose solution (range: 0–450 mg/dL, 0–25 mM) for 10 min. Each SERS measurement was made in the flow cell under saline with pH = 7.4, using $\lambda_{ex}$ = 632.8 nm, $P_{laser}$ = 2.5 mW, and $t$ = 30 s.

treat; zone E predictions lead to further aggravating abnormal glucose levels.

The EG3-modified AgFON sensor allows quantitative detection of glucose in the physiological range with a corresponding prediction error of 82 mg/dL (4.5 mM). In Fig. 8, 94% of the predictions fall in zones A and B, while a few data points overlap in zone D within the hypoglycemic area (<70 mg/dL, <3.9 mM). The error of 82 mg/dL (4.5 mM) can be partially attributed to variation in the nanoscale morphologies on different AgFON samples. The nanostructure on an AgFON substrate varies from point to point, affecting the localized surface plasmon resonance, and accordingly, the effective SERS enhancements.

While quantitative detection is an important characteristic of a viable biosensor, the sensors used in vivo, or even in complex in vitro media, such as in cellular cultures, must also be effective in the presence of interfering proteins. Serum albumin was used as a blood serum protein mimic to challenge the glucose sensor. The EG3-functionalized AgFON substrate was placed in a saline environment in a flow cell and the SERS spectrum was obtained (Fig. 9A). Then, a bovine serum albumin (BSA) solution was injected into the flow cell, and the SERS spectrum was collected throughout the 240-s incubation (Fig. 9B). Finally, the sample was exposed to 100 mM glucose, and the SERS spectrum was collected (Fig. 9C). Fig. 9D is the difference spectrum between 9B and 9A, demonstrating that BSA does not have a measurable

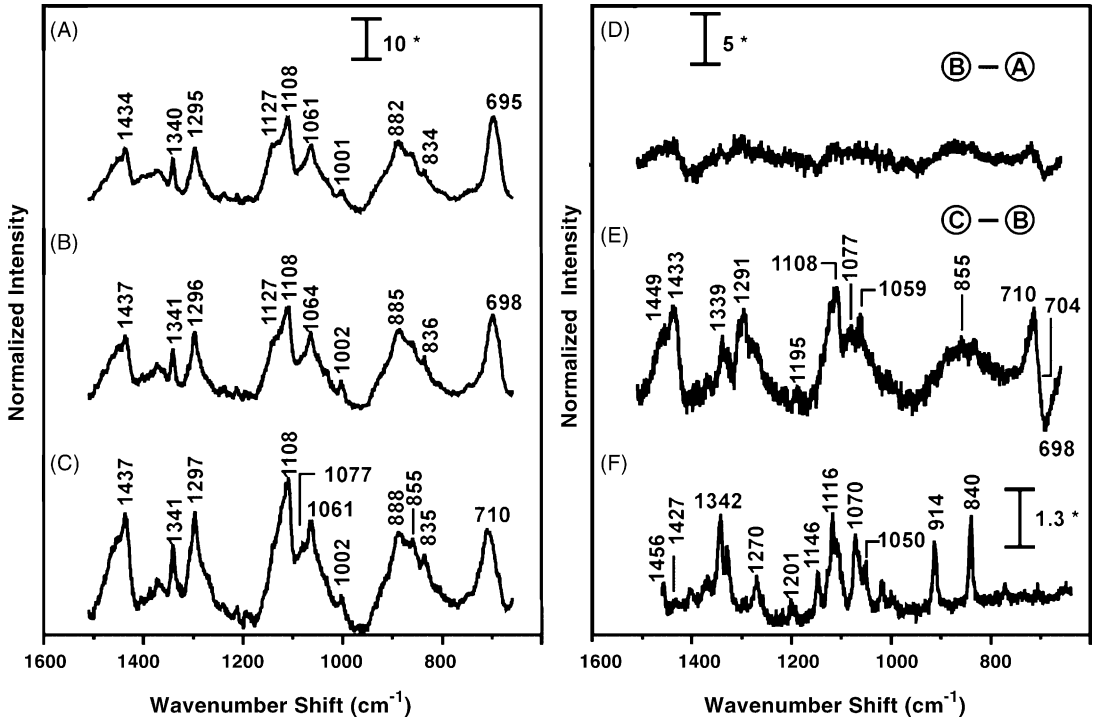


Fig. 9. SER spectra showing detection of glucose in presence of serum albumin. (A) EG3 monolayer on AgFON substrate, $\lambda_{ex}$ = 632.8, $P_{laser}$ = 0.8 mW, and $t$ = 240 s; (B) 1 mg/mL serum albumin injected into the flow cell to challenge the EG3-modified AgFON, $\lambda_{ex}$ = 632.8, $P_{laser}$ = 0.8 mW, and $t$ = 240 s; (C) 100 mM glucose injected into the flow cell, $\lambda_{ex}$ = 632.8, $P_{laser}$ = 0.8 mW, and $t$ = 240 s; (D) difference spectrum obtained by subtracting (A) from (B) revealing the lack of SERS spectrum for adsorbed serum albumin; (E) difference spectrum obtained by subtracting (B) from (C) indicating serum albumin exposure does not interfere with glucose detection; (F) normal Raman spectrum of crystalline glucose for comparison $\lambda_{ex}$ = 632.8, $P_{laser}$ = 5 mW, and $t$ = 30 s. (*) Denotes adu $mW^{-1}$ $s^{-1}$.

SERS spectrum. The lack of BSA SERS bands is likely due to inefficient adsorption of BSA to the EG3 partition layer. Fig. 9E demonstrates that the SERS glucose sensor is still effective after substrate exposure to an interfering protein, and that the peaks correspond with the crystalline glucose peaks shown in Fig. 9F. This experiment clearly indicates that glucose partitioning into EG3 is not influenced by the presence of large molecules, such as serum albumin.

In addition to demonstrating quantitative glucose detection in a clinically relevant concentration range and detection of glucose in the presence of other interfering proteins, other characteristics of the EG3-modified AgFON glucose sensor, such as durability and reusability, are demonstrated in published work [4].

## 4. Conclusion

Nanoscale optical sensors have potential utility in wide variety of applications. The inherently small size of the sensor and non-destructive nature of the optical measurement are significant advantages over macro-scale sensors, or other sensitive detection schemes that do not permit recovery of the analyte. We have demonstrated two types of nanosensors based on plasmonic phenomena, LSPR sensing, and SERS.

LSPR sensors operate by sensing change in local refractive index making them broadly applicable to a range of analytes. Specificity in these sensors can be designed by functionalizing the nanoparticles with appropriate receptor molecules. LSPR sensing can be monitored in real-time, e.g. for the monitoring of binding kinetics, and is a highly sensitive technique in both array (UV–vis) and single particle (dark-field transmission) format. The two illustrative examples of LSPR sensing show practical application, i.e. a non-model system, to biological a problem and to general chemical sensing. The dependence of the LSPR response to particle morphology permits the optimization of the sensors by careful control of size and shape during the fabrication process.

SERS, on the other hand, derives its selectivity in sensing by measuring the vibrational bands of the target molecule. Like LSPR, the SERS signal is highly dependent upon the substrate morphology. We have developed SERS-based sensors for two important target molecules: a *B. anthracis* biomarker and glucose in a serum protein mixture. For *B. anthracis*, SERS was used to directly measure the spores bound on the MFON substrate, whereas, glucose was detected by partitioning the carefully tailored alkanethiol derivative functionalized-MFON surface.

## Acknowledgements

This work was supported by the National Science Foundation (EEC-0118025, DMR-0076097, CHE-0414554), the Air Force Office of Scientific Research MURI program (F49620-02-1-0381), and the National Institutes of Health (1 R21 DK066990-01A1).

## References

[1] J. Ji, J.A. Schanzle, M.B. Tabacco, Anal. Chem. 76 (2004) 1411.
[2] F.S. Ligler, C.R. Taitt, L.C. Shriver-Lake, K.E. Sapsford, Y. Shubin, J.P. Golden, Anal. Bioanal. Chem. 377 (2003) 469.
[3] O. Kohls, T. Scheper, Sens. Actuators B 70 (2000) 121.
[4] C.R. Yonzon, C.L. Haynes, X. Zhang, 76 (2004) 78.
[5] A.J. Haes, W.P. Hall, L. Chang, W.L. Klein, R.P. Van Duyne, 4 (2004) 1029.
[6] H. Ho, M. Leclerc, J. Am. Chem. Soc. 126 (2004) 1384.
[7] S.L. Wiskur, E.V. Anslyn, J. Am. Chem. Soc. 123 (2001) 10109.
[8] G. Bauer, J. Hassmann, H. Walter, J. Haglmueller, C. Mayer, T. Schalkhammer, Nanotechnology (2003) 1289.
[9] C.L. Haynes, R.P. Van Duyne, J. Phys. Chem. B 105 (2001) 5599.
[10] U. Kreibig, M. Gartz, A. Hilger, Ber. Bunsen-Ges. 101 (1997) 1593.
[11] P. Mulvaney, MRS Bull. 26 (2001) 1009.
[12] M.A. El-Sayed, Acc. Chem. Res. 34 (2001) 257.
[13] S. Link, M.A. El-Sayed, J. Phys. Chem. B 103 (1999) 8410.
[14] U. Kreibig, M. Gartz, A. Hilger, H. Hovel, Adv. Met. Semicond. Clusters, vol. 4, JAI Press Inc., Stamford, 1998, p. 345.
[15] P. Mulvaney, Langmuir 12 (1996) 788.
[16] T.R. Jensen, K.L. Kelly, A. Lazarides, G.C. Schatz, J. Cluster Sci. 10 (1999) 295.
[17] T.R. Jensen, M.D. Malinsky, C.L. Haynes, R.P. Van Duyne, J. Phys. Chem. B 104 (2000) 10549.
[18] J. Yguerabide, E.E. Yguerabide, Anal. Biochem. 262 (1998) 157.
[19] S. Schultz, D.R. Smith, J.J. Mock, D.A. Schultz, P.N.A.S. 97 (2000) 996.
[20] G.C. Schatz, R.P. Van Duyne, Handbook of Vibrational Spectroscopy, vol. 1, Wiley, New York, 2002, p. 759.
[21] U. Kreibig, M. Vollmer, Optical Properties of Metal Clusters, Springer-Verlag, Heidelberg, Germany, 1995.
[22] C.R. Yonzon, E. Jeoung, S. Zou, G.C. Schatz, M. Mrksich, R.P. Van Duyne, J. Am. Chem. Soc. 126 (2004) 12669.
[23] A.J. Haes, S. Zou, G.C. Schatz, R.P. Van Duyne, J. Phys. Chem. B 108 (2004) 109.
[24] E.A. Smith, W.D. Thomas, L.L. Kiessling, R.M. Corn, J. Am. Chem. Soc. 125 (2003) 6140.
[25] B.T. Houseman, E.S. Gawalt, M. Mrksich, Langmuir 19 (2003) 1522.
[26] B.T. Draine, P.J. Flatau, J. Opt. Soc. Am. A (1994) 1491.
[27] B.T. Draine, P.J. Flatau, http://arxiv.org/abs/astro-ph/0309069, 2003.
[28] K.L. Kelly, E. Coronado, L. Zhao, G.C. Schatz, J. Phys. Chem. B 107 (2003) 668.
[29] A.J. Haes, R.P. Van Duyne, J. Am. Chem. Soc. 124 (2002) 10596.
[30] L.S. Jung, C.T. Campbell, T.M. Chinowsky, M.N. Mar, S.S. Yee, Langmuir 14 (1998) 5636.
[31] A.M. Michaels, M. Nirmal, L.E. Brus, J. Am. Chem. Soc. 121 (1999) 9932.
[32] J.J. Mock, D.R. Smith, S. Schultz, Nano Lett. 3 (2003) 485.
[33] J.J. Mock, S.J. Oldenburg, D.R. Smith, D.A. Schultz, S. Schultz, Nano Lett. 2 (2002) 465.
[34] T. Klar, M. Perner, S. Grosse, G. von Plessen, W. Spirkl, J. Feldmann, Phys. Rev. Lett. 80 (1998) 4249.
[35] Y. Matsuo, K. Sasaki, Jpn. J. Appl. Phys. 40 (2001) 6143.
[36] P.C. Lee, D. Meisel, 86 (1982) 3391.
[37] A.D. McFarland, R.P. Van Duyne, Nano Lett. 3 (2003) 1057.
[38] J.J. Mock, M. Barbic, D.R. Smith, D.A. Schultz, S.J. Schultz, J. Chem. Phys. 116 (2002) 6755.
[39] A.J. Haes, S. Zou, G.C. Schatz, R.P. Van Duyne, 108 (2004) 6961.
[40] M.D. Malinsky, K.L. Kelly, G.C. Schatz, R.P. Van Duyne, J. Am. Chem. Soc. 123 (2001) 1471.

[41] S. Soderholm, Y.H. Roos, N. Meinander, M. Hotokka, J. Raman Spectrosc. 30 (1999) 1009.
[42] R.L. McCreery, Raman Spectroscopy for Chemical Analysis, John Wiley & Sons Inc., New York, 2000.
[43] G.C. Schatz, R.P. Van Duyne, Electromagnetic Mechanism of Surface-Enhanced Spectroscopy, John Wiley & Sons Inc., New York, 2002.
[44] C.L. Haynes, R.P. Van Duyne, J. Phys. Chem. B 107 (2003) 7426.
[45] S. Nie, S.R. Emory, Science 275 (1997) 1102.
[46] K. Kneipp, Y. Wang, H. Kneipp, L.T. Perelman, I. Itzkan, R.R. Dasari, M.S. Feld, Phys. Rev. Lett. 78 (1997) 1667.
[47] J.M. Sylvia, J.A. Janni, J.D. Klein, K.M. Spencer, Anal. Chem. 72 (2000) 5834.
[48] S.C. Pinzaru, I. Pavel, N. Leopold, W. Kiefer, J. Raman Spectrosc. 35 (2004) 338.
[49] X. Zhang, M.A. Young, O. Lyandres, R.P. Van Duyne, J. Am. Chem. Soc. 127 (2004) 4484.
[50] C.R. Yonzon, C.L. Haynes, X. Zhang, J.T. Walsh, R.P. Van Duyne, Anal. Chem. 76 (2004) 78.
[51] A.M. Stacy, R.P. Van Duyne, Chem. Phys. Lett. 102 (1983) 365.
[52] G.J. Kovacs, R.O. Loutfy, P.S. Vincett, C. Jennings, R. Aroca, Langmuir 2 (1986) 689.
[53] L.A. Dick, A.D. McFarland, C.L. Haynes, R.P. Van Duyne, J. Phys. Chem. B 106 (2002) 853.
[54] X. Zhang, C.R. Yonzon, R.P. Van Duyne, 5221 (2003) 82.
[55] T.R. Jensen, R.P. Van Duyne, S.A. Johnson, V.A. Maroni, 54 (2000) 371.
[56] D.A. Stuart, C.R. Yonzon, X. Zhang, O. Lyandres, N. Shah, M.R. Glucksberg, J.T. Walsh, R.P. Van Duyne, Anal. Chem. 77 (2005) 4013.
[57] M. Litorja, C.L. Haynes, A.J. Haes, T.R. Jensen, R.P. Van Duyne, J. Phys. Chem. B 105 (2001) 6907.
[58] K.E. Shafer-Peltier, C.L. Haynes, M.R. Glucksberg, R.P. Van Duyne, J. Am. Chem. Soc. 125 (2003) 588.
[59] R. Goodacre, B. Shann, R.J. Gilbert, E.M. Timmins, A.C. McGovern, B.K. Alsberg, D.B. Kell, N.A. Logan, 72 (2000) 119.
[60] M.R. Jarvis, R. Goodacre, Anal. Chem. 76 (2004) 40.
[61] P. Carmona, 36A (1980) 705.
[62] P.A. Mosier-Boss, S.H. Lieberman, 54 (2000) 1126.
[63] S. Farquharson, A.D. Gift, P. Maksymiuk, F.E. Inscore, 58 (2004) 351.
[64] J.E. Chin, Control of Communicable Diseases Manual, American Public Health Association, Washington, DC, 2000.
[65] D. Blanco Gomis, J. Muro Tamayo, M. Alonso, Anal. Chim. Acta 436 (2001) 173.
[66] K.T. Carron, B.J. Kennedy, Anal. Chem. 67 (1995) 3353.
[67] L. Yang, E. Janle, T. Huang, J. Gitzen, P.T. Kissinger, M. Vreeke, A. Heller, Anal. Chem. 34 (1995) 1326.
[68] T.O. Deschaines, K.T. Carron, Appl. Spectrosc. 51 (1997) 1355.
[69] P. Freunscht, R.P. Van Duyne, S. Schneider, Chem. Phys. Lett. 281 (1997) 372.
[70] M.M. Walczak, C. Chung, S.M. Stole, C.A. Widrig, M.D. Porter, J. Amer. Chem. Soc. 113 (1991) 2370.
[71] E. Ostuni, R.G. Chapman, M.N. Liang, G. Meluleni, G. Pier, D.E. Ingber, G.M. Whitesides, Langmuir 17 (2001) 6336.
[72] J. Lahiri, L. Isaacs, J. Tien, G.M. Whitesides, Anal. Chem. 71 (1999) 777.
[73] S.L. Clark, P.T. Hammond, Adv. Mater. 10 (1998) 1515.
[74] K.L. Prime, G.M. Whitesides, J. Am. Chem. Soc. 115 (1993) 10714.
[75] M.A. Mauzac, N. Jozefonvicz, J. Biomater. 3 (1982) 221.
[76] J.H. Lee, J. Kopecek, J.D. Andrade, Biomed. Mater. Res. 23 (1989) 351.
[77] W.L. Clarke, D. Cox, L.A. Gonder-Frederick, W. Carter, S.L. Pohl, Diab. Care 10 (1987) 622.